RESEARCH ARTICLE

ADVANCED OPTICAL MATERIALS
www.advopticalmat.de

Surface-Enhanced Raman Scattering and Photothermal Effects on Optoplasmonic Nanofibers

*Gregory Q. Wallace, Emilie Ringe, Karen Faulds, Duncan Graham, and Jean-François Masson**

When decorated with plasmonic nanoparticles, pulled optical nanofibers are compatible with plasmonic techniques enabling the ability to probe microenvironments with high spatial and temporal resolution. Although the nanofibers exhibit excellent compatibility for biological samples including cells and tissues, the underlying interactions between the dielectric fiber, plasmonic nanoparticles, and the incident light have been minimally explored. It is shown that the complex coupling of optical and plasmonic properties within the nanofiber strongly influences both the surface-enhanced Raman scattering (SERS) and photothermal capabilities. Through a combination of experimental results and simulated electric field distributions and spectra it is demonstrated that, although the nanofibers may be homogeneously decorated with gold nanoparticles, the optical effects spatially differ. Specifically, the SERS performance varies periodically based on the diameter of the nanofiber, which is associated with ring resonator modes, while the photothermal effects are more homogeneous over the same diameters, highlighting differences in optoplasmonic properties at this length scale. Through understanding these effects, it may become possible to control temperatures and SERS properties to evaluate processes with micrometric spatial resolution, such as the analytes secreted during temperature-induced death of single cells.

1. Introduction

Plasmon-mediated spectroscopies, such as surface-enhanced Raman scattering (SERS), rely on interactions between incident light and the localized surface plasmon resonance (LSPR) of metallic nanostructures.[1] Upon excitation of the LSPR, nanoscale regions of electromagnetic (EM) enhancement, known as "hot-spots," form. When an analyte of interest is located within a hot-spot, its Raman signal undergoes remarkable enhancement. As a result, great effort is spent developing means of improving the SERS performance of nanoparticles (NPs) by increasing the number of hot-spots or the amount of EM enhancement. This is commonly achieved by preparing nanostructures that exhibit high intrinsic densities of hot-spots,[2,3] coupling NPs together to form dimers,[4,5] chains,[6,7] and ensembles;[8,9] or simply aggregating the NPs.[10–14] One of the many ongoing challenges of using these types of approaches is ensuring reproducibility both in the batch-to-batch synthesis as well as the SERS performance.[15]

As a result, alternative configurations involving the use of spherical NPs have been explored. One such design is the NP-on-mirror geometry,[16–19] where a metallic NP is added onto a metal-coated surface, and a strong hot-spot is formed in the junction between the metal film and the NP. This results in a more intense SERS response for analytes within the junction. By changing the nature of the particle, it is possible to improve the SERS signal. One such example is dielectric/metallic hybrid colloids that are composed of a gold dodecahedral NP that subsequently

G. Q. Wallace, J.-F. Masson
Département de Chimie
Institut Courtois
Centre Québécois des Matériaux Fonctionnels (CQMF) and
Regroupement Québécois des Matériaux de Pointe (RQMP)
Université de Montréal
C.P. 6128 Succ. Centre-Ville, Montréal, Québec H3C 3J7, Canada
E-mail: jf.masson@umontreal.ca

The ORCID identification number(s) for the author(s) of this article can be found under https://doi.org/10.1002/adom.202401640

DOI: 10.1002/adom.202401640

G. Q. Wallace, K. Faulds, D. Graham
Centre for Molecular Nanometrology
Department of Pure and Applied Chemistry
Technology and Innovation Centre
University of Strathclyde
99 George Street, Glasgow G1 1RD, United Kingdom

E. Ringe
Department of Material Science and Metallurgy
University of Cambridge
27 Charles Babbage Road, Cambridge CB3 0FS, United Kingdom

E. Ringe
Department of Earth Science
University of Cambridge
Downing Street, Cambridge CB2 3EQ, United Kingdom

has a SiO_2 sphere grown onto it.[20] With this geometry, the silica sphere acts as a "nanolens," focusing the incident light into, and collimating the scattered photons out of, the hot-spot. The coupling of photonic and plasmonic components is referred to as optoplasmonics.

It is important to recognize that different types of photonic and plasmonic components can be integrated into optoplasmonic designs.[21] The photonic components, include dielectric NP with high refractive indices, dielectric microcavities including whispering gallery mode and integrated ring resonators, dielectric waveguides, and photonic crystals. The principles of these various schemes as well as optoplasmonics in general have been discussed in greater detail in review articles.[22,23] Relevant to this work are instances where optoplasmonic systems are used for SERS. One approach is to have the optical and plasmonic components separated from each other in a dielectric-on-plasmonic approach. Examples of this scheme include TiO_2 spheres on gold NP (AuNP) clusters,[24] SiO_2 microsphere on a AuNP monolayer,[25] and SiO_2 microsphere on a deposited gold film.[26] Alternatively, the photonic component can be decorated with the plasmonic component as was shown for the gold dodecahedral NP-SiO_2 hybrid,[20] polystyrene microspheres coated with AuNPs that were subsequently deposited onto a thin gold film,[27] and more recently, SiO_2 microspheres decorated with AuNPs.[28]

Owing to the use of planar substrates in their preparation, these geometries are best suited for on-chip sensing. However, considerable focus is now being placed on the use of SERS for measurements involving biomaterials, such as live cells and tissues.[29] Interestingly, even though a variety of approaches for working with metallic NPs and biomaterials have been demonstrated, few of these exhibit compatibilities across different systems as many rely on targeted delivery of NPs. In this regard, alternative non-specific methods for positioning NPs are needed. The addition of metallic nanostructures onto dielectric supports with needle-like geometries offers such capabilities.[30] Herein, we refer to these as plasmonic nanofibers. The NPs are adsorbed onto the silica nanofiber, with the position of the plasmonic nanofiber controlled using an external device such as a piezoelectric positioning system,[31] or a micromanipulator.[32,33] Furthermore, because the tip and taper dimensions can be controlled, it is possible to insert plasmonic nanofibers into cells and tissues without causing unnecessary damage, while also being able to measure extracellular environments. As a result of this versatility, plasmonic nanofibers have been used to explore a variety of applications including the detection of neurotransmitter secretion[31] and metabolite gradients near cells,[34] sensing the extracellular and intracellular pH gradients of cancer cells[35] and live mice brains,[36] and the detection of heavy metal ions in breast cancer cells.[37] Interestingly, even with the various developments exploring the applications of plasmonic nanofibers, the underlying mechanisms behind the light-matter interactions of the plasmonic nanofibers have not been thoroughly evaluated. Understanding these interactions can provide insights into where the incident Raman light should be focused to maximize possible the SERS signal, as well as future nanofiber geometries, including the diameter of the taper.

Here, we investigate these interactions through a combination of 2D and 3D SERS measurements and finite-difference time-domain (FDTD) calculations. A focus is placed on understanding how these light-matter interactions influence the SERS and photothermal responses. For a presumed homogeneous distribution of NPs across a series of plasmonic nanofibers, the obtained SERS results show periodic intensity distributions across the length of the plasmonic nanofibers. This contrasts with the estimated temperature at the surface of the plasmonic nanofibers, which even though uses a temperature-sensitive Raman reporter, shows a more homogeneous response. Given the nano- to microscale diameters of the tip and taper of the plasmonic nanofibers, aided by the FDTD calculations and dark field measurements, we draw parallels to the phenomena described in optoplasmonics to better understand the light-matter interactions. Specifically, the strong relationship between the diameter of the plasmonic nanofiber with respect to the diffraction-limited spot size of the incident laser. Overall, this work provides new insights into plasmonic nanofibers, especially the geometries that may serve best for applications in SERS-based sensing.

2. Results and Discussion

2.1. Geometry and Structural Properties of Plasmonic Nanofibers

Plasmonic nanofibers are an optoplasmonic system composed of a dielectric photonic component (borosilicate glass fiber), and a plasmonic aspect (AuNPs). When using a laser-puller, the dimensions of the nanofiber (i.e., tip diameter and taper length) can be adjusted by varying the parameters used.[38] The introduction of plasmonic nanostructures can be achieved by evaporating a thin layer of metal onto the surface, or through the adsorption of NPs onto the surface using either classical silane chemistry,[39] or a block-copolymer brush layer.[40] In this work, the latter approach was used, the details of which are provided in the Experimental Section.

A schematic representation of a AuNP decorated plasmonic nanofiber is shown in **Figure 1**A. Here, four distinct regions have been highlighted, though depending on the tip geometry and the wavelength of the excitation light, these regions may or may not be present. Region i) corresponds to the area closest to the tip. Within this region, the diameter of the nanofiber is smaller than the diffraction-limited spot of the incident light, whereas in region ii) the diameters are comparable to and slightly greater than the diffraction-limited spot of the incident and Raman scattered photons. Moving further up the tip, the domains iii) and iv) have fiber diameters that are larger and much larger than the diffraction-limited spots for the wavelength of light used, respectively. Representative SEM images of a plasmonic nanofiber across domains i–iii) are shown in Figure 1B–D. As demonstrated in the inset of Figure 1D, the AuNPs are well distributed across the surface of the nanofiber with minimal aggregation. For the purposes of better understanding the light-matter interactions of the plasmonic nanofiber, spherical AuNPs were used, though other structures can be readily added to the surface.

Extending across the plasmonic nanofiber, the geometry of the taper can be observed, (Figure S1, Supporting Information), with a cone angle of 2° to 3° being estimated. With an intact tip, it takes tens of microns of lateral movement to reach a tip diameter of ≈1 µm. As mentioned, this is the initial region of the nanofiber most relevant for measurements inside cells. For cell secretion experiments, given the angle of the fiber when mounted onto

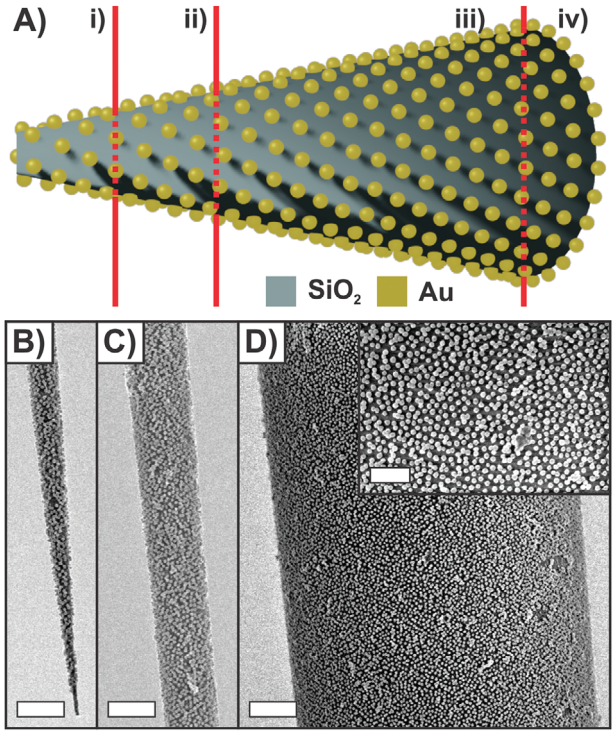

Figure 1. A) Schematic representation of a plasmonic nanofiber composed of a SiO_2 nanofiber decorated with AuNPs. The plasmonic nanofiber is subdivided into different regions corresponding to diameters i) below, ii) comparable to, iii) larger than, and iv) considerably larger than the diffraction-limited Raman laser spot. B–D) SEM images of a plasmonic nanofiber decorated with AuNPs. These images highlight the AuNP distribution in regions i–iii. The scale bars in (B–D) are 1 µm and the scale bar in the inset of (D) is 500 nm.

a micromanipulator or piezoelectric positioner, the range of applicability extends a bit further down the plasmonic nanofiber. Given the challenges of detection in tissue, having a wider portion of the nanofiber is advantageous as it becomes easier to focus once inserted into the tissue.[32] For context, the span covering 1–3 µm in diameter, which covers a range of ≈3–10 × the diffraction-limited spot size of a 633 nm excitation, spans a length of ≈35 µm.

2.2. Surface-Enhanced Raman Scattering Performance of Plasmonic Nanofibers

With an aim to better understand the SERS performance of the nanofibers, including where it is best to focus the incident laser light, plasmonic nanofibers were functionalized with 4-mercaptobenzonitrile (4-MBN). 4-MBN was chosen as the probe molecule because it has a series of intense vibrational modes that span from 550 to 2250 cm^{-1} (**Figure** 2A). Therefore, for the 633 nm excitation wavelength used throughout this work, the Raman scattered photons will have wavelengths ranging from 656 to 738 nm. This broad spectral range of vibrational modes is ideal for evaluating optical coupling that may occur when using nanofibers as opposed to planar surfaces.

SERS maps were taken with a step size of 0.5 and 1 µm in the x and y axes respectively (Figures 2B,C). Though a shorter step size may be beneficial, overexposure of the plasmonic nanofiber becomes a risk as the incident laser had a spot size of ≈1 µm. To account for the varying diameters potentially influencing the ideal focus, SERS maps were acquired at different z depths. Furthermore, to ensure that the various regions of interest were evaluated, the length of the SERS maps was at least 100 µm in length. SERS maps were generated by plotting the intensities for the five main peaks of 4-MBN. Although it is possible to readily distinguish where the plasmonic nanofiber is with respect to the map, the SERS response is far from uniform. In fact, it appears as if there are distinct bands of high and low intensity across the length of the nanofiber.

Previous mapping at the tip of a plasmonic nanopipette, made of a SiO_2 capillary as opposed to a SiO_2 rod, showed a heterogeneous response,[41] but those were prepared using aminosilane chemistry as opposed to the block-copolymer method. Given that the block-copolymer approach yields a more homogeneous coating of the AuNPs and improved SERS sensitivity compared to the aminosilane approach,[40] the presence of periodically varying SERS intensities across multiple nanofibers is counterintuitive (Figure S2, Supporting Information). To better illustrate the relative fluctuations, line scans were taken along the length of the plasmonic nanofibers across a series of depths (Figure 2D–F; Figure S3, Supporting Information). One potential explanation is that the SERS response for NPs intrinsically varies and that at the single-particle level, encountering SERS-inactive NPs is common.[42] Furthermore, a large increase in the SERS response could be attributed to intense coupling between adjacent AuNPs.[43] The former is something that cannot be helped and may play a role in the minimal SERS response near the tips of the nanofibers as these areas would have the fewest AuNPs being illuminated. If the cause was due to the presence of intense EM field coupling or aggregation, then the regions of intense SERS signals would likely be small and encompass just a few pixels. Since the bands of differing intensity were observed independently of the focus of the laser and the uniform coating of the AuNPs, the bands likely originate from optical effects from the curved tip.

2.3. Theoretical Optoplasmonic Properties of Decorated Silica Spheres

To better understand the observed optical effects in the SERS spectra, finite-difference time-domain (FDTD) calculations were performed to separate out contributions from the curved silica surface and the AuNPs. SiO_2 microparticles (µPs) are a commonly used structure for optoplasmonic studies,[20,25–28,44] with both experimental and theoretical optical properties having been established. Relative to the tapered geometry of the plasmonic nanofibers, SiO_2 µPs can be more readily modeled with defined dimensions, allowing for an initial understanding of potential optical effects to be established, especially for a structure that is decorated all over with AuNPs.

As a first approximation, the wavelength-dependent electric field intensity was plotted for a series of SiO_2 spheres with diameters ranging from 0.5 to 3 µm (Figure S4, Supporting Information). These diameters were chosen as they represent dimensions indicated in Figure 1A, across diameters from sub-diffraction

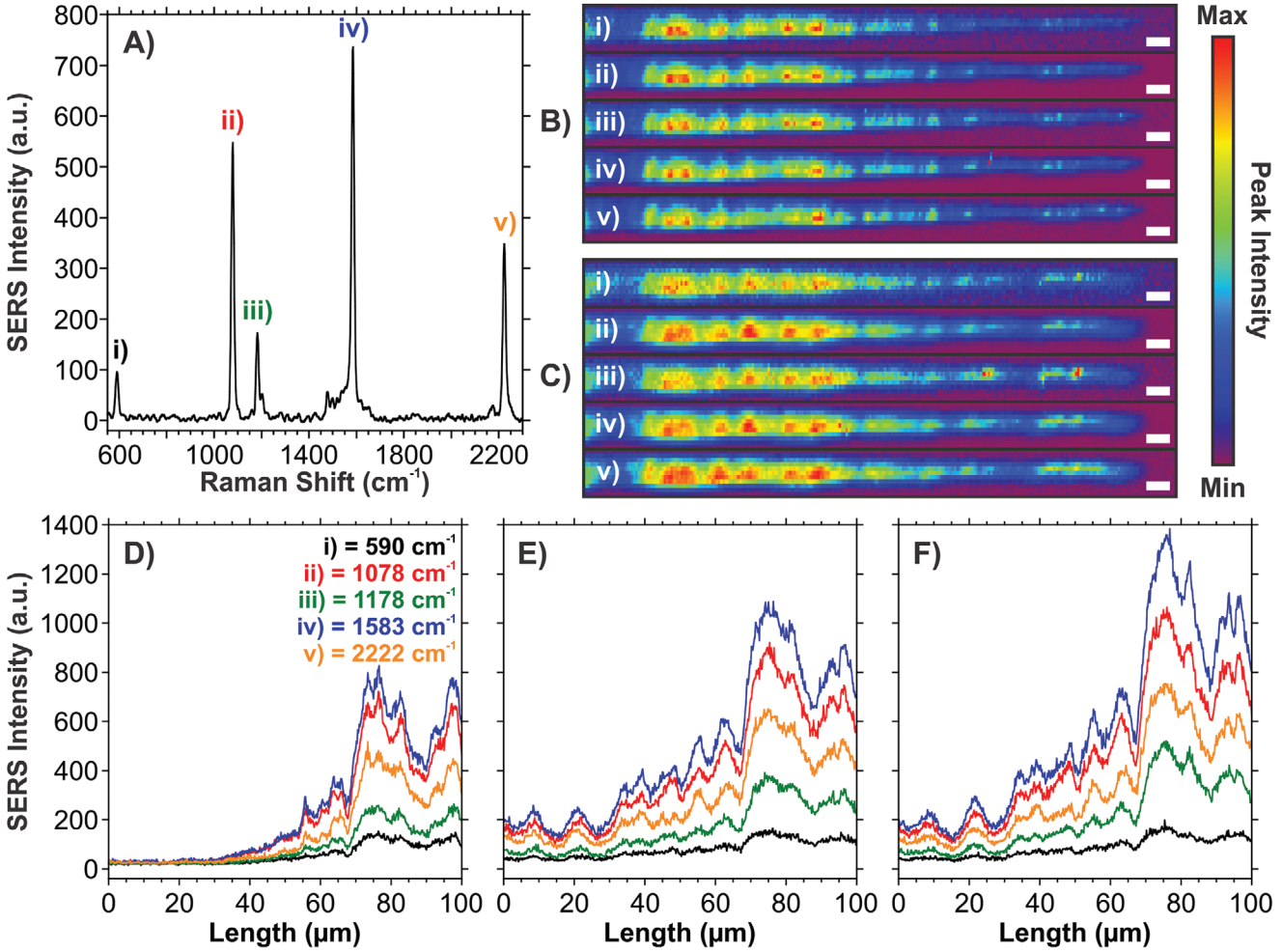

Figure 2. A) SERS spectrum of 4-MBN adsorbed onto the AuNPs of a plasmonic nanofiber. B,C) SERS maps taken of a 4-MBN functionalized plasmonic nanofiber at *z* depths 5 μm apart. The numbers i–v) correspond to the vibrational modes indicated in (A). The intensity scale of the maps corresponds to the minimum and maximum values from each map. Step sizes of 0.5 and 1 μm were used in the *x* and *y* axes respectively. The scale bars indicate 5 μm. D–F) SERS intensity line scans across a different plasmonic nanofiber at different *z* depths. For the line scans, a step size of 0.2 μm was used.

limited to a few times the diffraction limit. As the diameter of the SiO_2 spheres increases, the number of observable optical ring modes increases along with the quality factor. Fundamentally, when the excitation wavelength used matches one of these resonances, the light couples to the surface of the sphere, and circumnavigates the surface multiple times. As seen in Videos S1 and S2 (Supporting Information), for an undecorated and a AuNP decorated 2000 nm diameter SiO_2 sphere respectively, there is also a delay between the light traveling around the surface compared to the light traveling through the sphere. As the diameter changes, this effect becomes even greater (Videos S3 and S4, Supporting Information). Under these conditions, as the light travels around the dielectric sphere, additional opportunities exist for the incident light to be able to excite the LSPR of nanostructures. For well-established ring resonator geometries, the increased interactions occur through the formation of an evanescent field,[45] such as those at the surface of the dielectric microsphere.[46]

When decorated with AuNPs, as **Figure 3** shows, even though the LSPR of the AuNPs is near 540 nm, there is an amplification of the optical modes associated with the SiO_2 μP. There is also a slight red shift in the optical modes, which can be attributed to the small increase in overall diameter once decorated with the AuNPs as well as the corresponding change in refractive index. As opposed to having the AuNPs only at the base of the μP, the presence of AuNPs over the surface offers additional opportunities to excite the LSPR as the light travels around the μP (Videos S5 and S6, Supporting Information). Beyond enhancing the optical modes, the SiO_2 μP acts as a ball lens. Under these conditions, the incident light is focused onto the AuNPs nearer to the base of the structure, and the scattered photons are then focused backward to the light source. As such, the collection efficiency of the scattered photons is improved.[28]

2.4. Theoretical Optoplasmonic Properties of Plasmonic Nanofibers

Although SiO_2 spheres can be helpful for establishing a fundamental understanding of the optoplasmonic interactions, it is necessary to extend the calculations to a cylindrical geometry to

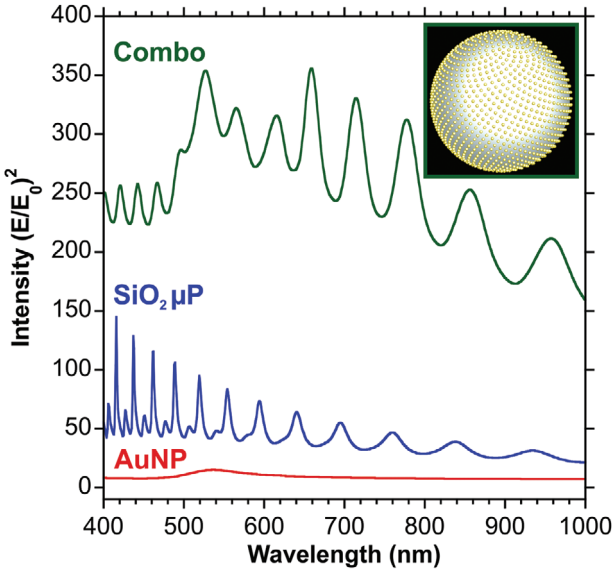

Figure 3. Finite-difference time-domain (FDTD) calculated wavelength-dependent electromagnetic field intensities for 50 nm AuNPs, a 2000 nm diameter SiO_2 microparticle (μP), and the SiO_2 μP decorated with the AuNPs arranged in a Fibonacci spiral configuration (Combo). The electric field intensities were determined by placing a monitor 1 nm away from the AuNP surface along the axis of the polarization, the base of the SiO_2 μP, and the bottom most AuNP, respectively.

better reflect the structure of the nanofiber. Furthermore, unlike the SiO_2 spheres where a Fibonacci spiral could be used to create a theoretical coating, alternative arrangements of AuNPs on the surface of a SiO_2 cylinder had to be considered. A comparison of different arrangements showed that although the values for the observed electric field intensity did vary, in general, the optical trends remained similar (Figure S5, Supporting Information). That is when a high density of AuNPs was used along with the presence of multiple rings of AuNPs, the optical modes were enhanced (Figure S6, Supporting Information). To further validate the model, alternative nanofiber diameters were explored whereby the diameter was changed in 25 nm increments. Here, noticeable changes were observed in the calculated electric field intensities (**Figure 4**), especially at the base of the plasmonic nanofiber (P2) compared to the top (P1). Here, the top of the structure corresponds to the side of the plasmonic nanofiber nearest to the excitation source. At the bottom of the plasmonic nanofiber, the optical modes are more intense but are less well-defined. Instead of appearing as narrow bands, a broader continuum-like band was observed. Whereas at the top of the structure, the bands appeared to be more discrete. These differences arise from the directional incident coupling of light in the spherical structure (Figure 4A), where the simulated spectra from the top part are essentially described by the convolution of the plasmon response (P1) and ring resonator modes (P2). The bottom of the structure has stronger light coupling from the lensing effect, explaining the higher intensity of the response and its coupling with the ring resonator modes describes the optical response seen at P4. Although the substrate is physically symmetrical, these observations indicate that the top and bottom side optically differ.

The calculations of Figure 4 were for a region of the nanofiber where the diameter would be several times larger than the diffraction-limited spot size of the incident Raman light. Similar calculations were performed across a wide range of diameters, with similar trends being observed (Figure S7, Supporting Information). To ascertain if other optical phenomena may also be occurring, electromagnetic field intensity maps for a 633 nm excitation wavelength were calculated for different sizes (**Figure 5**). As was carried out for the spheres, the diameters covered dimensions that were shorter than, and up to several times greater than the diffraction limit spot size of the incident 633 nm light. While the wavelength-dependent calculations provide insight into the behavior of the optical modes, the electric field maps demonstrate the light-matter interactions. The electromagnetic field maps of Figure 5 shows that when the diameter of the nanofiber is smaller than the excitation wavelength (Figure 5A,B), then there is no appearance of a "photonic nanojet," or lensing effect. As the diameter increases, then additional enhancement appears at the base of the nanofiber (Figure 5D–F). Enhancement is also observed at the top of the structure, best exemplified by Figure 5E. These calculations further support past descriptions of the nanofibers acting as a ball lens, when the diameter of the nanofiber is sufficiently large.

2.5. Optoplasmonic Properties of Plasmonic Nanofibers

Simulations predicted that lensing and optical resonances should be observed on the nanofibers, and experimental Raman maps showed periodic regions of high intensity. Correlations between theory and experimental evidence were then made from the SEM images, SERS images, and visible spectra collected with hyperspectral dark-field microscopy on individual nanofibers. The SERS maps and correlated SEM images of Figure 3 and Figure S1 (Supporting Information) allowed the diameter of the nanofibers to be calculated, where high-intensity SERS was observed from the fiber tip to ≈3 μm, while the hyperspectral dark-field images provided spectral information at different nanofiber diameters. Applying a ring resonator model can predict optical resonances in curved surfaces (Equation 1).

$$m\lambda = 2\pi r n_{eff} \quad (1)$$

where m is the order of the mode, λ is the laser wavelength (632.8 nm), r is the radius of the fiber and n_{eff} is the refractive index approximated to the one of glass (1.457). The experimentally observed regions of high SERS were in strong agreement with the theoretically predicted resonances for ring resonator modes for the 632.8 nm excitation laser (Figure S8, Supporting Information), where the experimental resonances are within a range of less than 4% of the predicted diameter for resonances on two different fibers. The resonator modes are also wavelength dependent, so the fiber diameter at which resonances occur could be Raman shift dependent if the Raman scattered photons enter ring resonances prior to collection. However, there is no apparent shift in resonance diameter in Figure 2E, which shows different Raman bands of 4-MBN. This result can be explained by the likely scenario that only the intense laser beam enters the resonance. Alternatively, the Raman scattered photons may enter resonance,

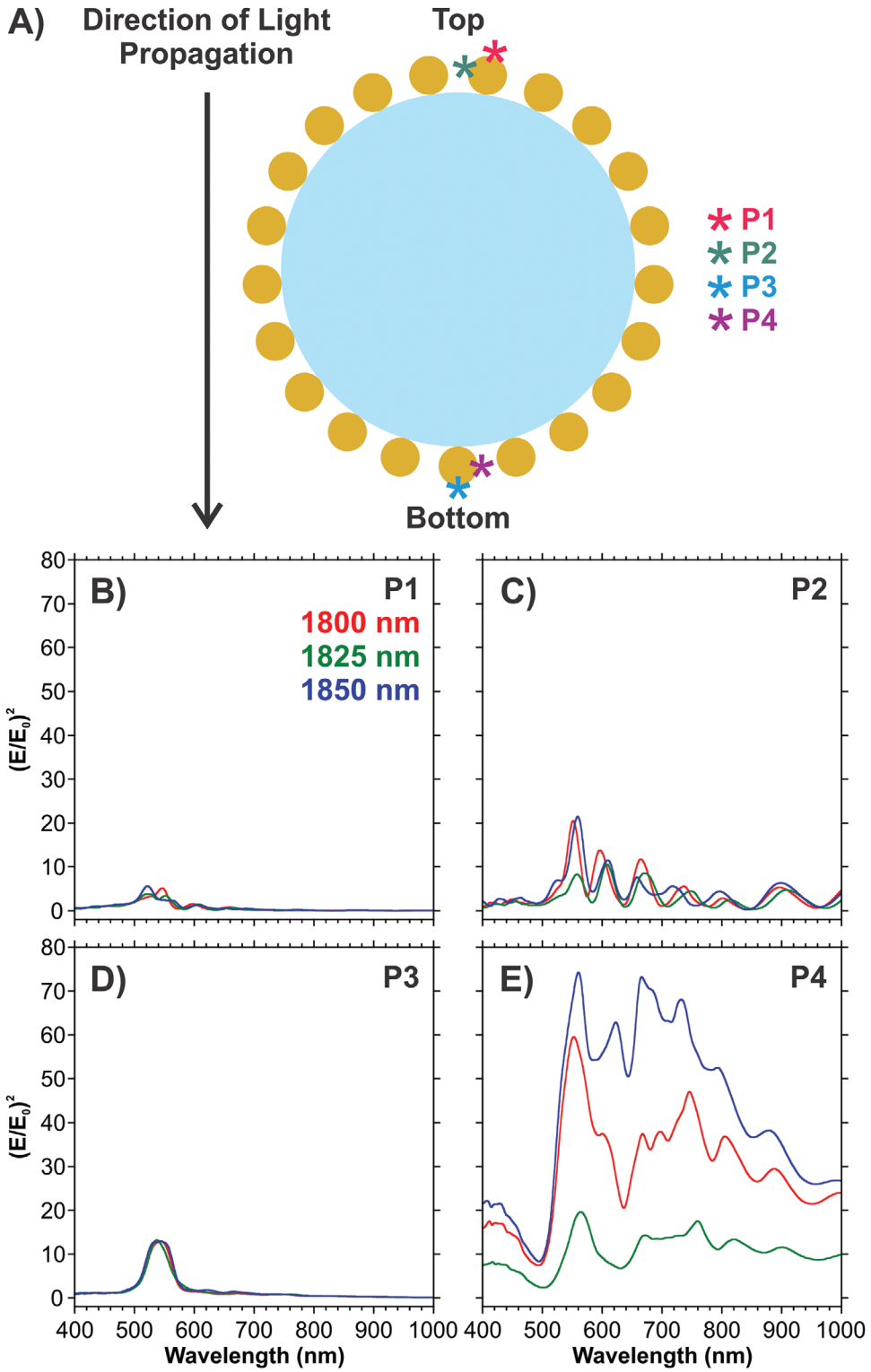

Figure 4. A) Representative schematic detailing where the electric field monitors are positioned with respect to a SiO_2 rod decorated with AuNPs and the direction of light propagation indicated. The top of the rod corresponds to the area nearest to the plane wave light source, and the bottom is the furthest away from it. B–D) FDTD calculated wavelength-dependent electromagnetic field intensities taken at the top and bottom of an 1800, 1825, and 1850 nm diameter SiO_2 rod decorated with AuNPs.

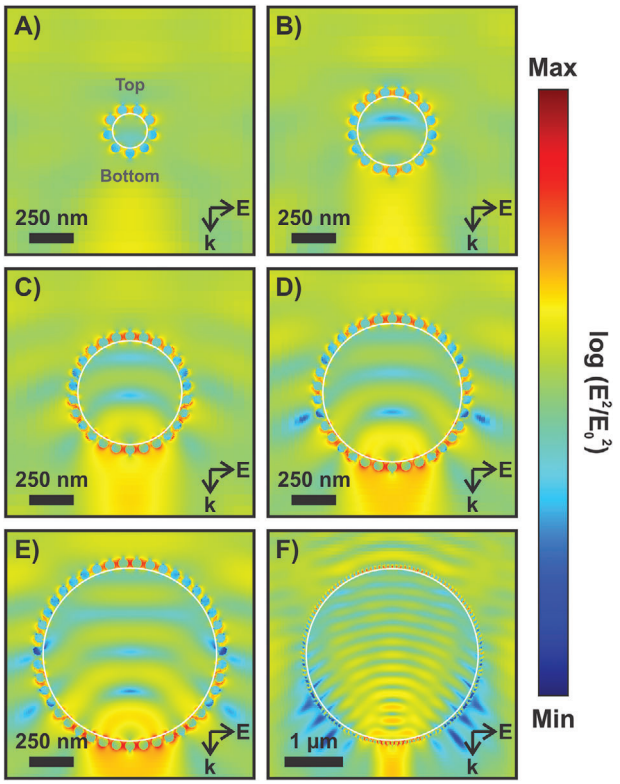

Figure 5. Normalized FDTD calculated electromagnetic field maps showing the distribution of enhancement at 633 nm for plasmonic nanofibers where the SiO_2 rods have diameters of A) 200, B) 400, C) 600, D) 800, E) 1000, and F) 3000 nm. An indication of the top and bottom of the structure with respect to the position of the incident light source is indicated in (A).

but the image resolution of the SERS maps is insufficient to resolve the small variations of the predicted resonance diameter of ≈10–15% (Figure S9, Supporting Information).

Further evidence that resonator modes control the spatial distribution of the SERS signal was obtained from the spectral resonances observed by dark-field hyperspectral microscopy. A series of higher-intensity bands were observed in spectra collected at specific diameters on AuNPs-coated nanofibers or bare nanofibers (**Figure 6**, red spectra). These resonances correlated well with the predicted ring resonator modes for a given nanofiber diameter, with an example given in Table S1 (Supporting Information) for a larger fiber diameter where more resonances are observed. Interestingly, the spectra changed depending on where they were collected along the cross-section of the fiber, with some regions (black traces in Figure 6) appearing as a peak between 600 and 700 nm, and other locations showing the ring resonator modes convoluted into the lamp profile. The control spectra on bare nanofibers (black trace, Figure 6B) showed no profile associated with optoplasmonic coupling. Specifically, no increase in the optical modes as predicted by FDTD calculations (Figures 3 and 4), or resemble either of the representative spectra shown in Figure 6A. Additional spectral evidence is provided in Figure S10 (Supporting Information). Taken together, these results clearly show that regions of high SERS intensity on the SERS maps correspond to the excitation of ring resonator modes. There are additional factors that may need to be considered. It has previously been shown that for structures with a cone geometry,[47] such as a taper, higher-order whispering gallery modes can be excited. These modes may also be a contributing factor, as was shown for tip-shaped silicon metasurfaces that were decorated with AuNPs which exhibited an improved SERS response.[48]

2.6. Photothermal Performance of Plasmonic Nanofibers

Over the course of evaluating the detection of neurotransmitter secretion, observations of photothermal damage to the cells were noticed.[31] Other observations for the generation of heat at the surface of the nanofiber include the formation of bubbles in solution (Figure S11 and Video S7, Supporting Information), and melting of the plasmonic nanofiber tip when the experiments were performed in air (Figure S11, Supporting Information). Therefore, although increasing the incident laser power may be helpful to try and overcome interference from biological samples, such as tissues, it may have a negative impact on the nanofibers due to excessive heat generation.

Estimating the temperature at the surface of plasmonic nanostructures can be achieved by developing a calibration curve based on the anti-Stokes to Stokes ratio,[49,50] or by using a temperature-sensitive analyte.[51–53] In the latter approach, for gold nanostructures,[54] derivatives of phenyl isocyanide have shown promise.[28,52,55] The work of Ngo et al., is of note as they investigated the photothermal effects of gold nanorods adsorbed onto pulled nanofibers.[55] However, the authors were focused primarily on the tip of their plasmonic nanofibers as that is what was inserted into the cells and tumors. Given the varying SERS performance as shown in Figure 2, we sought to evaluate if the SERS response for 4-fluorophenyl isocyanide (4-FPIC) and estimated surface temperature would undergo similar trends.

The spectra of **Figure 7**A,B demonstrate the characteristic trends associated with the use of 4-FPIC as a temperature-sensitive analyte. As the laser power increases, there is a distinct shift in the spectral position of the CN vibrational mode, while the other vibrational modes remain similar. In this instance, a 12 cm^{-1} shift, which is based on the previously reported shift of ≈0.2 cm^{-1} $°C^{-1}$,[52,55] indicates a temperature increase of ≈60 °C. Figure 7A also highlights that if the laser power is sufficiently high, additional peaks will appear in the spectra, and can be attributed to the molecular degradation at the surface of the AuNPs.

As was observed throughout the previous SERS mapping experiments, there also appear to be bands of varying SERS intensities along the length of the plasmonic nanofiber (Figure 7C,D). When the relative positions of the CN peaks are plotted for pixels where the CN vibrational mode met a threshold intensity of 100 a.u., it is clear that as the laser power is increased, the CN peak shifts (Figure 7E,F). Importantly, owing to the sub 1 mW laser power used, there does not appear to be any damage to the plasmonic nanofiber (Figure 7G). When these iso-Raman shift maps are compared to a wider portion of the plasmonic nanofiber, where the diameter is large enough that a 40×40 μm^2 region can be imaged (effectively a planar surface), the same degree of shift is not observed (Figure S12, Supporting Information). As such, the plasmonic nanofibers appear to have superior photothermal properties near the tapered region compared

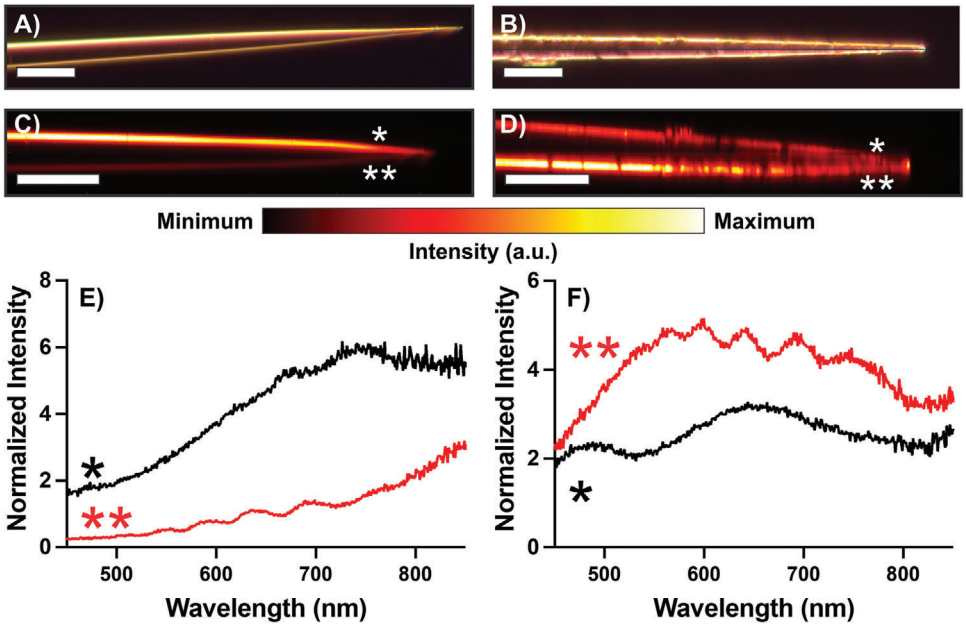

Figure 6. Dark field images of A) bare, and B) plasmonic nanofibers. Corresponding dark field total intensity obtained from the spectral camera of the C) bare, and D) plasmonic nanofibers. Dark-field spectra were collected at different locations on a nanofiber cross-section as indicated in C and D for the E) bare, and F) plasmonic nanofibers. The scale in the images is 20 μm.

to wider portions but do not require that a sub-diffraction limited tip be present (Figure S13, Supporting Information).

Interestingly, the shift in the CN peak corresponding to the increase in temperature does not appear to follow the periodic increase in the SERS intensity. This could be attributed to the fact that not all the AuNPs support SERS, but the majority will support a thermal response. Furthermore, it was previously shown that for aggregated structures,[56] it is the number of AuNPs present that influenced the temperature increase as opposed to the coupling between the adjacent structures which led to the increase in the SERS signal. Thus, the photothermal response may occur independently of the optical modes present within the system. Here, it is important to remember that heat transfer to the surrounding medium is a non-radiative decay process that occurs at the time scale of hundreds of picoseconds to nanoseconds.[57,58] By contrast, at a 1 μm diameter, it takes ≈10 fs for the light to travel around the circumference. Owing to the delay between the excitation of the LSPR and the dissipation of the energy by heat, the benefit of having the incident light coupled with optical modes is minimized. Instead, the light is predominantly focused by the curvature of the nanofiber, independently of the presence of optical modes. This lensing effect, or the focusing of light, may also play a role in the increased temperature estimated near the taper of the plasmonic nanofiber compared to the flatter regions. Microbubble formation has previously been reported for semi-ordered arrangements of AuNPs on planar surfaces.[59] It is important to recognize that heat dissipation requires transfer to the surrounding medium as well as the substrate. At the narrow regions of the plasmonic nanofiber, not only can the entirety of the plasmonic nanofiber be within the confocal volume of the incident beam, but with such a small volume of substrate present, poor heat dissipation may occur. This would result in higher temperatures, which when coupled with even higher laser powers, yield the photothermal damage shown in Figure S11 (Supporting Information).

3. Conclusion

How the incident light couples into the plasmonic nanofiber is heavily dependent on where on the nanofiber the measurement is occurring. Diameters that are smaller than the diffraction-limited spot size behave differently than those that are comparable to or just a few times larger than it, which behave very differently to the wide diameters which in effect act almost as a planar surface. At or near the tip of the nanofiber, the optical coupling whether via a lens-based effect or through optical ring modes, appears to be minimal.

For SiO_2 μPs, diameters in the range of 4–5 μm have been found to be ideal for maximizing optoplasmonic coupling for SERS-based measurements.[28] With the plasmonic nanofibers, the optical coupling in the SERS measurements is dominated by diameters matching the ring resonator modes associated with the incident Raman beam. The lensing capabilities of the plasmonic nanofibers then allow for the Raman scattered photons to be better directed toward the collection source. Whereas in photothermal heating, the heat generated is less dependent on coupling with optical modes, though lensing may still play a role.

Overall, plasmonic nanofibers are an interesting and developing approach for performing highly localized measurements. Successfully exploiting the various optical coupling regimes will allow for even further advancements, especially in instances where combining SERS-based measurements with local heating would be beneficial, such as single-cell apoptosis and necrosis. Furthermore, examining different taper geometries as well as means of coupling the incident light with the nanofiber may allow for improved sensing and heating capabilities.

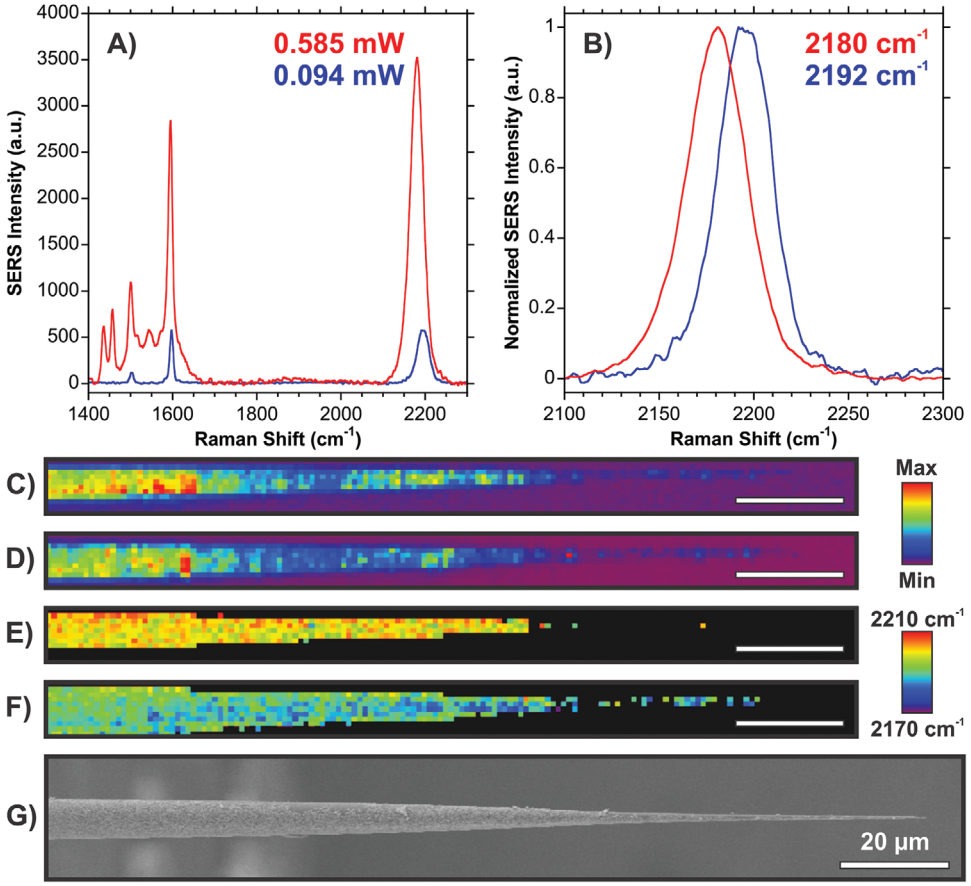

Figure 7. A) SERS spectrum of 4-FPIC adsorbed onto the AuNPs of a plasmonic nanofiber taken at two laser powers. B) Normalized SERS intensities of the CN group with the Raman shift for the maximum intensity indicated. SERS maps indicate the minimum and maximum intensities of the CN vibrational mode at C) 0.094, and D) 0.585 mW. Corresponding distributions for the peak position of the CN group for pixels with intensities greater than 100 a.u. for excitation laser powers of E) 0.094, and F) 0.585 mW. G) SEM image taken of the plasmonic nanofiber after the completion of the mapping experiments.

4. Experimental Section

Materials: The PS-P4VP diblock copolymer [Mn(PS) = 41 kg mol^{-1}, Mn(P4VP) = 20 kg/mol, Mw/Mn = 1.18] was purchased from Polymer Source Inc. THF (99.99%) was obtained from VWR. Gold chloride trihydrate ($HAuCl_4 \cdot 3H_2O$, ≥99.9%) and sodium hydroxide (NaOH) were purchased from Sigma–Aldrich. Trisodium citrate dihydrate (≥99%), hydrogen peroxide (H_2O_2, 30%) sulfuric acid (H_2SO_4), hydrochloric acid (HCl, 37%), and nitric acid (HNO_3, 68–70%) were acquired from Fischer Scientific. 4-mercaptobenzonitile (4-MBN) was obtained from Toronto Research Chemicals. 4-fluorophenyl isocyanide (4-FPIC) was purchased from Fisher Scientific. Borosilicate glass rods (1 mm diameter, 10 cm length) were purchased from World Precision Instruments and Sutter Instruments. Milli-Q water with a resistivity of 18.2 MΩ·cm was used for the preparation of NP solutions.

Synthesis of Gold Nanoparticles (AuNPs): Glassware and magnetic stir bars were cleaned using aqua regia (HCl/HNO_3, 3:1 v/v), rinsed using NaOH, and then finally Milli-Q water prior to use. *Caution: aqua regia is highly corrosive and must be handled with caution*. Ultraviolet–vis–near-infrared (UV-vis-NIR) spectra of the prepared AuNP solutions were acquired using an Agilent Technologies Cary 500 UV–vis–NIR spectrophotometer. Citrate-stabilized AuNPs were synthesized using a kinetically controlled seeded growth method.[60] Briefly, 150 mL of 2.2 mM sodium citrate was added to a 250 mL round-bottom flask. The solution was heated in an oil bath to boiling under vigorous stirring with a reflux condenser attached. After boiling was maintained for 10 min, 1 mL of a 25 mM $HAuCl_4$ solution was added, and boiling was allowed to continue for 10 additional minutes. The solution of the seeds was then cooled to 90 °C and allowed to equilibrate for 10 min. Then, 1 mL of the 25 mM $HAuCl_4$ solution was added and allowed to react for 30 min. This process was completed for two more additions, after which, ≈55 mL of the solution was removed and replaced with 53 mL of Milli-Q water and 2 mL of a 60 mM sodium citrate solution. This solution became the seed solution, and three additional growth steps were performed. Extinction spectra were acquired throughout the process, to ensure that the final AuNP solution exhibited an LSPR between 533 and 536 nm (Figure S14, Supporting Information). Once the desired LSPR position was achieved, the AuNP solution was cooled to room temperature and was subsequently stored at 4 °C.

Preparation of Plasmonic Nanofibers: Pulled nanofibers were obtained by pulling borosilicate glass rods with a P-2000 laser puller (Sutter Instrument, California) using a two-line program with instrument-specific parameters. For tip diameters of ≈200 nm: Line 1) Heat: 280, Filament: 0, Velocity: 15, Delay: 200, Pull: 20, Line 2) Heat: 350, Filament: 0, Velocity: 15, Delay: 128, Pull: 150.

The protocol for converting the nanofibers to plasmonic nanofibers employed the use of a block-copolymer brush film.[40] Nanofibers were initially immersed in ethanol for 5 min followed by freshly prepared piranha solution (H_2SO_4:H_2O_2, 7:3 v/v) at 90 °C for 60 min, then thoroughly rinsed with Milli-Q water and dried under vacuum for 60 min. *Caution: piranha solution is highly corrosive and must be handled with caution.*

A 0.05 mg mL^{-1} solution of the PS-P4VP di-block copolymer in THF was prepared. The clean and hydrophilic nanofibers were dipped into the polymer solution using a dip-coater (KSV3000 Langmuir–Blodgett) at a speed of 51.4 mm min^{-1}. After an incubation time of 3 min, the now polymer-coated nanofibers were removed from the polymer solution at the same rate, placed into a Petri dish, covered, and allowed to dry. The polymer-coated nanofibers were stored in the dark at 4 °C until use. To make the polymer-coated nanofibers SERS active, the previously described AuNPs must be added to the surface by electrostatic interactions. The AuNPs were concentrated by a factor of 2 or 3 and redispersed in a 3 mM solution of trisodium citrate. The pH of the AuNP solutions was subsequently lowered to ≈4.5 using HCl. The polymer-coated nanofibers were immersed in the desired AuNP solutions for 3 h. The AuNP-coated nanofibers, referred to here as plasmonic nanofibers, were washed with Milli-Q water to remove unbound AuNPs and gently dried with air.

Functionalization of Plasmonic Nanofibers: The plasmonic nanofibers were subsequently immersed in either ethanolic solutions of 1 mM 4-MBN or 0.1 mM FPIC for 3 h. *Caution: FPIC is highly toxic and must be handled inside a fume hood*. Functionalized plasmonic nanofibers were then gently rinsed with ethanol and dried under nitrogen.

Surface-Enhanced Raman Scattering Measurements: SERS spectra for the FPIC functionalized samples were performed with a Renishaw InVia Raman microscope controlled by Wire 4.4. The microscope was equipped with a 633 nm laser and a Leica N Plan EPI 50× microscope objective (NA = 0.75). Under these conditions, the laser had a spot size of ≈1 µm. A 1200 grooves/mm grating and an acquisition time of 1 s were used for all measurements. Step sizes in the maps varied between 0.5 and 1 µm in the *x* and *y* axes to minimize oversampling. All SERS spectra and maps were processed by using a custom Python script. The laser power at the same was measured with a Thorlabs power meter (PM100D) equipped with an S130C 400–1100 nm sensor.

Dark-Field Measurements: Hyperspectral dark-field images were obtained with a Nikon Eclipse Ti microscope equipped with a tungsten lamp, an Isoplane 320 spectrophotometer (Princeton Instruments), and a Princeton Instrument ProEM HS 1024 × 1024 EMCCD. An S Plan Fluor ELWD 40× objective (NA = 0.6) was used for imaging the pulled fibers. The dark-field condenser (Nikon TI-DF dry condenser) had a NA of 0.8–0.95. Data was processed using MatLab R2020a and with GraphPad Prism.

Finite-Difference Time-Domain Calculations: Finite-difference time-domain (FDTD) calculations were performed using a commercial software FDTD solution (Ansys Lumerical FDTD). For the calculations, air was chosen as the surrounding medium. A plane wave excitation source was used for calculations involving incident light, and a point source for calculating effects associated with Raman scattered photons. Owing to the variety of dimensions and geometries evaluated, the meshing parameters varied considerably. In general, higher-resolution meshes were used near the most important AuNPs, those at the very top and bottom of the SiO_2 microparticles or rods. Custom scripts (available upon request) were used to position the AuNPs either in a Fibonacci spiral geometry on the SiO_2 spheres or, distributed evenly in rows (SiO_2 rods). Perfectly matched layers were used in all axes, and Johnson and Christy dielectric values for gold.

Characterization of Plasmonic Nanofibers: Plasmonic nanofibers were imaged using either a JEOL JSM-7400F field-emission scanning electron microscope (SEM) operated with an accelerating voltage of 3 kV, or an FEI QEMSCAN 650F using 15 kV and a high vacuum to image the samples. Samples were placed on carbon tape to minimize charging, and no coating was deposited on the substrates.

Supporting Information

Supporting Information is available from the Wiley Online Library or from the author.

Acknowledgements

The authors acknowledge the financial support of the Natural Science and Engineering Research Council of Canada (grant number RGPIN/03114-2021), Fonds de Recherche du Québec—Nature et Technologies (grant number 181843), Fonds de Recherche du Québec—Santé (grant number 271793), The Royal Society, UK, International Exchange Scheme (IES\R3\203092), the Leverhulme Trust (grant number RPG-2020-400), and the EU Framework Programme for Research and Innovation Horizon 2020 (ERC Starting Grant SPECs 804523).

Conflict of Interest

The authors declare no conflict of interest.

Data Availability Statement

The data that support the findings of this study are available from the corresponding author upon reasonable request.

Keywords

finite-difference time-domain, optoplasmonics, photothermal, plasmonic nanofibers, surface-enhanced Raman scattering

Received: June 19, 2024
Revised: August 12, 2024
Published online:

[1] X. X. Han, R. S. Rodriguez, C. L. Haynes, Y. Ozaki, B. Zhao, *Nat. Rev. Methods Primers* **2022**, *1*, 87.
[2] T. V. Tsoulos, S. Atta, M. J. Lagos, M. Beetz, P. E. Batson, G. Tsilomelekis, L. Fabris, *Nanoscale* **2019**, *11*, 18662.
[3] J. Ma, X. Liu, R. Wang, J. Zhang, P. Jiang, Y. Wang, G. Tu, *ACS Appl. Nano Mater.* **2020**, *3*, 10885.
[4] P. A. Mercadal, E. R. Encina, E. A. Coronado, *J. Phys. Chem. C* **2019**, *123*, 23577.
[5] J. Li, T. S. Deng, X. Liu, J. A. Dolan, N. F. Scherer, P. F. Nealey, *Nano Lett.* **2019**, *19*, 4314.
[6] R. W. Taylor, R. Esteban, S. Mahajan, J. Aizpurua, J. J. Baumberg, *J. Phys. Chem. C* **2016**, *120*, 10512.
[7] Z. Yin, Y. Wang, C. Song, L. Zheng, N. Ma, X. Liu, S. Li, L. Lin, M. Li, Y. Xu, W. Li, G. Hu, Z. Fang, D. Ma, *J. Am. Chem. Soc.* **2018**, *140*, 864.
[8] M. J. Jeon, X. Ma, J. U. Lee, H. Roh, C. C. Bagot, W. Park, S. J. Sim, *J. Phys. Chem. C* **2021**, *125*, 2502.
[9] G. Qi, D. Wang, C. Li, K. Ma, Y. Zhang, Y. Jin, *Anal. Chem.* **2020**, *92*, 11755.
[10] A. Y. F. Mahmoud, C. J. Rusin, M. T. McDermott, *Analyst* **2020**, *145*, 1396.
[11] Y. Zhou, J. Liu, T. Zheng, Y. Tian, *Anal. Chem.* **2020**, *92*, 5910.
[12] H. T. Phan, T. S. Heiderscheit, A. J. Haes, *J. Phys. Chem. C* **2020**, *124*, 14287.
[13] M. Liu, F. Wang, X. Zhang, X. Mao, L. Wang, Y. Tian, C. Fan, Q. Li, *Nat. Protoc.* **2021**, *16*, 383.
[14] J. Fergusson, G. Q. Wallace, S. Sloan-Dennison, R. Carland, N. C. Shand, D. Graham, K. Faulds, *J. Phys. Chem. C* **2023**, *127*, 24475.
[15] D. B. Grys, R. Chikkaraddy, M. Kamp, O. A. Scherman, J. J. Baumberg, B. de Nijs, *J. Raman Spectrosc.* **2021**, *52*, 412.
[16] W. Lum, I. Bruzas, Z. Gorunmez, S. Unser, T. Beck, L. Sagle, *J. Phys. Chem. Lett.* **2017**, *8*, 2639.
[17] K. Zhang, Y. Liu, Y. Wang, R. Zhang, J. Liu, J. Wei, H. Qian, K. Qian, R. Chen, B. Liu, *ACS Appl. Mater. Interfaces* **2018**, *10*, 15388.
[18] L. T. M. Huynh, S. Yoon, *J. Phys. Chem. C* **2018**, *122*, 26047.
[19] Y. Li, S. Tang, S. Xu, Z. Duan, Z. Wang, Y. Zhang, *ACS Appl. Nano Mater.* **2020**, *3*, 5116.

[20] M. Kamp, B. de Nijs, N. Kongsuwan, M. Saba, R. Chikkaraddy, C. A. Readman, W. M. Deacon, J. Griffiths, S. J. Barrow, O. S. Ojambati, D. Wright, J. Huang, O. Hess, O. A. Scherman, J. J. Baumberg, *Proc. Natl. Acad. Sci. U.S.A.* **2020**, *117*, 14819.
[21] Y. Hong, B. M. Reinhard, *J. Opt.* **2019**, *21*, 113001.
[22] Y. Hong, B. M. Reinhard, *J. Opt.* **2019**, *21*, 113001.
[23] Y. Chen, Y. Yin, L. Ma, O. G. Schmidt, *Adv. Opt. Mater.* **2021**, *9*, 2100143.
[24] Y. Hong, M. Pourmand, S. V. Boriskina, B. M. Reinhard, *Adv. Mater.* **2013**, *25*, 115.
[25] Y. Hong, X. Zhou, B. Xu, Y. Huang, W. He, S. Wang, C. Wang, G. Zhou, Y. Chen, T. Gong, *ACS Appl. Mater. Interfaces* **2020**, *12*, 24192.
[26] L. Ju, J. Shi, C. Liu, Y. Huang, X. Sun, *Spectrochim. Acta A* **2021**, *255*, 119698.
[27] J. Qian, Z. Zhu, J. Yuan, Y. Liu, B. Liu, X. Zhao, L. Jiang, *Nanosc. Adv.* **2020**, *2*, 4682.
[28] J. F. Masson, G. Q. Wallace, J. Asselin, A. Ten, M. Hojjat Jodaylami, K. Faulds, D. Graham, J. S. Biggins, E. Ringe, *ACS Appl. Mater. Interfaces* **2023**, *15*, 46181.
[29] G. Q. Wallace, J. F. Masson, *Analyst* **2020**, *145*, 7162.
[30] M. Chisanga, J. F. Masson, *Annu. Rev. Anal. Chem.* **2024**, *17*, 313.
[31] F. Lussier, T. Brulé, M. J. Bourque, C. Ducrot, L. É. Trudeau, J. F. Masson, *Faraday Discuss.* **2017**, *205*, 387.
[32] G. Q. Wallace, B. Delignat-Lavaud, X. Zhao, L. É. Trudeau, J. F. Masson, *J. Chem. Phys.* **2020**, *153*, 124702.
[33] J. Wang, Y. Geng, Y. Shen, W. Shi, W. Xu, S. Xu, *Sens. Actuators B-Chem.* **2019**, *290*, 527.
[34] F. Lussier, D. Missirlis, J. P. Spatz, J. F. Masson, *ACS Nano* **2019**, *13*, 1403.
[35] X. Zhao, S. Campbell, G. Q. Wallace, A. Claing, C. G. Bazuin, J. F. Masson, *ACS Sens.* **2020**, *5*, 2155.
[36] W. Wang, F. Zhao, M. Li, C. Zhang, Y. Shao, Y. Tian, *Angew. Chem., Int. Ed.* **2019**, *58*, 5256.
[37] X. Zhao, S. Campbell, P. Z. El-Khoury, Y. Jia, G. Q. Wallace, A. Claing, C. G. Bazuin, J. F. Masson, *ACS Sens.* **2021**, *6*, 1649.
[38] K. Lim, S. Goines, M. Deng, H. McCormick, P. J. Kauffmann, J. E. Dick, *Analyst* **2023**, *148*, 2992.
[39] A. N. Shipway, E. Katz, I. Willner, *ChemPhysChem* **2000**, *1*, 18.
[40] H. Zhu, F. Lussier, C. Ducrot, M. J. Bourque, J. P. Spatz, W. Cui, L. Yu, W. Peng, L. É. Trudeau, C. G. Bazuin, J. F. Masson, *ACS Appl. Mater. Interfaces* **2019**, *11*, 4373.
[41] J. F. Masson, J. Breault-Turcot, R. Faid, H. P. Poirier-Richard, H. Yockell-Lelièvre, F. Lussier, J. P. Spatz, *Anal. Chem.* **2014**, *86*, 8998.
[42] M. Liebel, I. Calderon, N. Pazos-Perez, N. F. van Hulst, R. A. Alvarez-Puebla, *Angew. Chem., Int. Ed.* **2022**, *61*, e202200072.
[43] S. Y. Ding, E. M. You, Z. Q. Tian, M. Moskovits, *Chem. Soc. Rev.* **2017**, *46*, 4042.
[44] M. L. Gorodetsky, A. D. Pryamikov, V. S. Ilchenko, *J. Opt. Soc. Am. B* **2000**, *17*, 1051.
[45] I. M. White, J. Gohring, X. Fan, *Opt. Express* **2007**, *15*, 17433.
[46] I. White, X. Fan, in *Proc. SPIE 5994, Chemical and Biological Sensors for Industrial and Environmental Security*, Society of Photo-Optical Instrumentation Engineers (SPIE), Bellingham, WA, USA **2005**, 5994G.
[47] M. Sumetsky, *Opt. Lett.* **2011**, *36*, 145.
[48] A. Lagarkov, I. Boginskaya, I. Bykov, I. Budashov, A. Ivanov, I. Kurochkin, I. Ryzhikov, I. Rodionov, M. Sedova, A. Zverev, A. K. Sarychev, *Opt. Express* **2017**, *25*, 17021.
[49] S. Park, G. J. Yeon, H. Lee, H. H. Shin, Z. H. Kim, *J. Phys. Chem. C* **2022**, *126*, 451.
[50] Z. Yu, R. R. Frontiera, *ACS Nano* **2023**, *17*, 4306.
[51] P. Li, S. H. C. Askes, E. del Pino Rosendo, F. Ariese, C. Ramanan, E. von Hauff, A. Baldi, *J. Phys. Chem. C* **2023**, *127*, 9690.
[52] S. Hu, B. J. Liu, J. M. Feng, C. Zong, K. Q. Lin, X. Wang, D. Y. Wu, B. Ren, *J. Am. Chem. Soc.* **2018**, *140*, 13680.
[53] K. Chen, H. Wang, *Nano Lett.* **2023**, *23*, 2870.
[54] D. Prezgot, J. Cruikshank, M. Makila-Boivin, S. Birgani, A. Ianoul, *Spectrochim. Acta A* **2022**, *280*, 121514.
[55] D. N. Ngo, V. T. T. X. Ho, G. Kim, M. S. Song, M. R. Kim, J. Choo, S. W. Joo, S. Y. Lee, *Anal. Chem.* **2022**, *94*, 6463.
[56] Z. C. Zeng, H. Wang, P. Johns, G. V. Hartland, Z. D. Schultz, *J. Phys. Chem. C* **2017**, *121*, 11623.
[57] E. L. Keller, N. C. Brandt, A. A. Cassabaum, R. R. Frontiera, *Analyst* **2015**, *140*, 4922.
[58] K. O. Aruda, M. Tagliazucchi, C. M. Sweeney, D. C. Hannah, E. A. Weiss, *Phys. Chem. Chem. Phys.* **2013**, *15*, 7441.
[59] G. Baffou, J. Polleux, H. Rigneault, S. Monneret, *J. Phys. Chem. C* **2014**, *118*, 4890.
[60] N. G. Bastús, J. Comenge, V. Puntes, *Langmuir* **2011**, *27*, 11098.